

RESEARCH ARTICLE

10.1002/2015JC011105

Special Section:

Forum for Arctic Modeling
and Observing Synthesis
(FAMOS): Results and
Synthesis of Coordinated
Experiments

Key Points:

- A full range of double-diffusive processes are analyzed in an Arctic eddy
- Double-diffusive staircases are not present in regions of high shear
- Eddy decay is influenced by both double-diffusive and turbulent mixing

Correspondence to:

Y. Bebieva,
yana.bebieva@yale.edu

Citation:

Bebieva, Y., and M.-L. Timmermans (2016), An examination of double-diffusive processes in a mesoscale eddy in the Arctic Ocean, *J. Geophys. Res. Oceans*, 121, 457–475, doi:10.1002/2015JC011105.

Received 3 JUL 2015

Accepted 11 DEC 2015

Accepted article online 15 DEC 2015

Published online 13 JAN 2016

An examination of double-diffusive processes in a mesoscale eddy in the Arctic Ocean

Yana Bebieva¹ and Mary-Louise Timmermans¹

¹Department of Geology and Geophysics, Yale University, New Haven, Connecticut, USA

Abstract Temperature and salinity measurements of an Atlantic Water mesoscale eddy in the Arctic Ocean's Canada Basin are analyzed to understand the effects of velocity shear on a range of double-diffusive processes. Double-diffusive structures in and around the eddy are examined through the transition from low shear (outside the eddy and within its solid body core) to high geostrophic shear zones at the eddy flanks. The geostrophic Richardson number takes large values where a double-diffusive staircase is observed and lowest values at the eddy flanks where geostrophic velocity is largest and a well-formed staircase is not present. A Thorpe scale analysis is used to estimate turbulent diffusivities in the flank regions. Double-diffusive and turbulent heat, salt, and buoyancy fluxes from the eddy are computed, and used to infer that the eddy decays on time scales of around 4–9 years. Fluxes highlight that Atlantic Water heat within the eddy can be fluxed downward into deeper water layers by means of both double-diffusive and turbulent mixing. Estimated lateral variations in vertical fluxes across the eddy allow for speculation that double diffusion speeds up the eddy decay, having important implications for the transfer of Atlantic Water heat in the Arctic Ocean.

1. Introduction

The vertical temperature and salinity structure in the upper Arctic Ocean consists of warm and salty waters derived from the Atlantic Ocean underlying relatively cooler, fresher water modified by fresh river influxes, surface buoyancy forcing, and Pacific Ocean influxes. In the Canada Basin, the warm core of the Atlantic Water (AW) layer centers around 400 m depth. Although there is a large amount of heat stored in the AW layer, in the central basins, this heat is insulated from the surface ocean (and sea-ice cover) by the strong Arctic halocline stratification. In the central basins, vertical heat transport from the AW is due largely to double-diffusive fluxes, which have been studied extensively [e.g., Neal and Neshyba, 1973; Perkin and Lewis, 1984; Padman and Dillon, 1987, 1988; Timmermans et al., 2008a]. It is generally found that vertical double-diffusive heat fluxes are only a small fraction of ocean-to-ice heat fluxes. There may be a role for turbulent fluxes; Padman and Dillon [1989] analyzed thermal microstructure measurements in the Canada Basin double-diffusive staircase, pointing out the presence of breaking internal waves (shear-driven instabilities) in the staircase. They showed depth ranges of disturbed step structures and speculated that in the long-term average, shear-driven mixing may have important consequences for heat and salt fluxes (although this could not be quantified given the limitations of their data).

Double diffusion occurs when temperature and salinity effects on density oppose each other while the stratification is statically stable, and arises because the molecular diffusivity of heat is nearly 2 orders of magnitude larger than that of salt [Stern, 1960]. If both temperature and salinity increase with depth (e.g., in the upper portion of the AW layer in the Arctic Ocean), then the potential energy required to maintain the double-diffusive instability is derived from the destabilizing temperature component of density. This type of double-diffusive convection is referred to as diffusive convection (DC) and is associated with a DC staircase (a series of homogeneous layers in temperature and salinity separated by sharp gradients in temperature and salinity). The other type of double diffusion arises when temperature and salinity both decrease with depth (i.e., the salinity component of density is destabilizing) and is associated with salt fingers (SF), or an SF staircase. The SF type of double diffusion is less common in the Arctic; however, at the base of the AW layer, there are occasionally density stable regions with a structure prone to SF, which can be associated with AW eddies as will be shown later in this paper. Further, the SF type of double diffusion plays a role in the propagation of Arctic-

wide thermohaline intrusions. These intrusions are centered around the core of the AW, and consist of alternating DC and SF regions in depth. Thermohaline intrusions propagate laterally across entire Arctic basins driven in part by a net loss of buoyancy [e.g., Carmack *et al.*, 1998; Merryfield, 2002; Woodgate *et al.*, 2007]. A comprehensive review of double-diffusive processes is given by Radko [2013].

In the central Canada Basin, parameterized double-diffusive heat fluxes [Kelley, 1990] from the upper part of the AW through the DC staircase are consistent with molecular heat fluxes across staircase interfaces [Padman and Dillon, 1987; Timmermans *et al.*, 2008a]. Double-diffusive fluxes are at least an order of magnitude smaller than ocean-to-ice heat fluxes (0.2 W/m^2 compared to several W/m^2), and the individual mixed layers in the DC staircase (of several meters in thickness) are laterally coherent across hundreds of kilometers [Timmermans *et al.*, 2008a]. The DC staircase appears to persist in a variety of environments ranging from quiescent to weakly turbulent [Padman and Dillon, 1987; Melling *et al.*, 1984; Timmermans *et al.*, 2008a]. However, the influence of shear-driven turbulent mixing in determining the presence or absence of a well-defined double-diffusive staircase in the Arctic Ocean has not been quantified. Mesoscale eddies offer a chance to explore the influence of velocity shear on double-diffusive processes.

Mesoscale eddies may be an important source of shear-driven mixing in the Arctic Ocean. Observational studies indicate a substantial number of mesoscale eddies at all depths, which influence the lateral transport of properties such as heat, momentum, and nutrients [e.g., Manley and Hunkins, 1985; Pickart *et al.*, 2005; Timmermans *et al.*, 2008b; Dmitrenko *et al.*, 2008; Carpenter and Timmermans, 2012; Zhao *et al.*, 2014; Watanabe *et al.*, 2014]. Eddies in the AW layer derive from the AW boundary current and feature double-diffusive structures [e.g., Woodgate *et al.*, 2001; Dmitrenko *et al.*, 2008]. Dmitrenko *et al.* [2008] analyzed an AW eddy on the Laptev Sea continental slope and showed that the temperature and salinity properties of the eddy evolve predominantly by vertical double-diffusive fluxes (dominated by salt-finger fluxes), with turbulent fluxes driving property evolution in its deeper portion.

Here we investigate the detailed structure of an anticyclonic eddy consisting of a warm AW core sampled in September 2005 in the northwest Canada Basin. Study of the eddy provides a means to examine how double-diffusive processes depend on varying temperature and salinity gradients and the geostrophic shear associated with its presence. A previous study has examined double-diffusive structures in the presence of an eddy (having relatively cool and fresh core waters) in the eastern Caribbean Sea to assess possible staircase formation mechanisms [Morell *et al.*, 2006]. The coarse horizontal sampling in Morell *et al.* [2006] precluded inferences of a definitive relation between the double-diffusive staircase, lateral temperature and salinity gradients, and shear associated with the eddy, although their results suggest a staircase present at its flanks and less well-defined steps in its core. These results imply that the presence of the eddy is associated with anomalous core temperature-salinity values and vertical density ratio amenable to double diffusion, while the shear associated with the eddy azimuthal velocity was not sufficiently strong to prevent well-defined double-diffusive structures from forming.

In general, the central Arctic Ocean, where double-diffusive mixing features prominently, is an environment of weak turbulent mixing because sea-ice coverage for most of the year limits the penetration of wind-energy input to the upper ocean [e.g., Halle and Pinkel, 2003]. Along the boundaries of the Arctic basins, mixing levels are higher [e.g., Melling *et al.*, 1984; Rippeth *et al.*, 2015], and double-diffusive staircases are not observed. Elsewhere in the world ocean, several studies have examined the situation of shear-driven turbulent mixing and double-diffusive mixing operating concurrently. Analysis of microstructure data (and shadowgraph images of optical microstructure) from the North Atlantic Tracer Release Experiment (NATRE), showed that even in the absence of a well-defined SF staircase, double-diffusive mixing may still persist along with turbulent mixing [St. Laurent and Schmitt, 1999]. Low dissipation rates measured during the C-SALT experiment in the tropical North Atlantic indicated smaller buoyancy fluxes through an SF staircase in the presence of shear-driven turbulence compared to those inferred from double-diffusive parameterizations for pure SF fluxes [Gregg and Sanford, 1987]. Our investigation of double-diffusive structures concurrently with an AW eddy provides a means to explore the transition between predominantly double-diffusive mixing (in the ambient water and eddy core) and turbulent mixing (around the eddy flanks) without needing microstructure measurements, which can be difficult to obtain in the ice-covered Arctic.

This paper is organized as follows. In the next section, we describe the measurements and basic water-column structure. We examine temperature and salinity measurements from an Ice-Tethered Profiler (ITP)

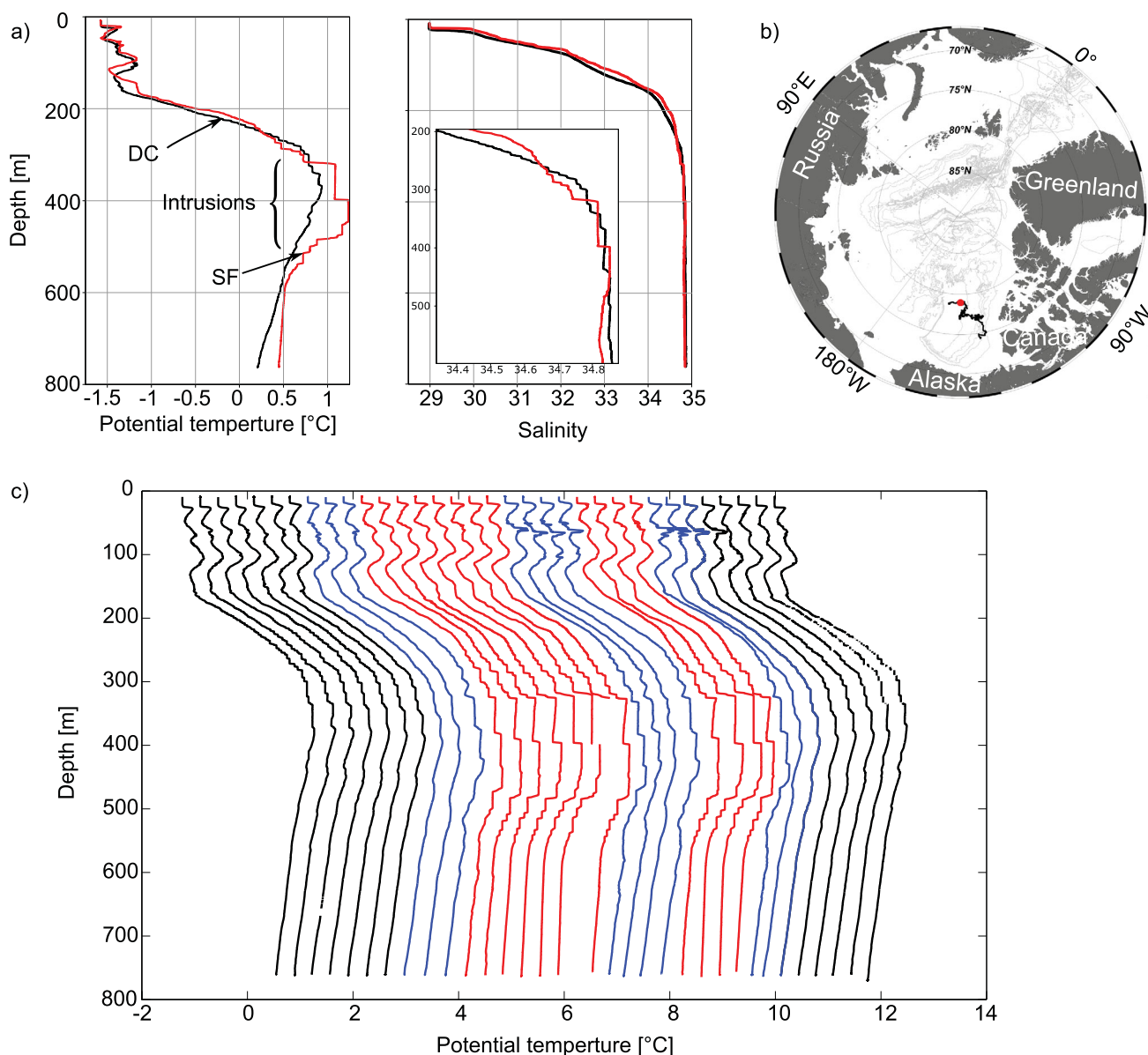


Figure 1. (a) Potential temperature (referenced to the surface) and salinity profiles measured by ITP 1: typical Canada Basin profile away from the eddy (black lines, 15 September 2005); profile through the eddy core (red lines, 23 September 2005). (b) Map showing locations of ITP 1 profiles over the course of its drift, with the eddy location marked by the red dot. (c) Sequence of potential temperature profiles through the eddy from 15 September 2005 to 2 October 2005. Each profile is offset by 0.34°C from the left-most profile. Blue profiles are from the eddy flank regions; red profiles are in the vicinity of the eddy core; black profiles are nominally ambient waters.

that drifted in the Canada Basin and transected an anticyclonic mesoscale eddy in the AW layer. We characterize the basic eddy structure (including radius and azimuthal velocities) in section 3. In section 4, we characterize the range of double-diffusive structures within the eddy, and in section 5, we show how double-diffusive structures may be influenced by the geostrophic shear associated with the eddy. Turbulent and double-diffusive fluxes are estimated and their relative roles are assessed in section 6 where we also speculate on eddy decay time scales. Findings are summarized and discussed in section 7.

2. Ice-Tethered Profiler Measurements and Water-Column Structure

Temperature and salinity measurements from an ITP (ITP system number 1) that operated in the Canada Basin in 2005–2007 are analyzed here (Figure 1b). An ITP is an automated profiling system deployed in the sea ice that provides year-round CTD measurements (temperature, salinity, and pressure with accuracies of

$\pm 0.001^\circ\text{C}$, ± 0.005 and ± 1 dbar, respectively) from several meters beneath the sea ice to 750 m depth [Krishfield *et al.*, 2008; Toole *et al.*, 2011]. The CTD system profiles on a tether that is suspended below a surface float in the sea ice, and data are relayed via underwater modem to the surface float, from which they are transmitted to shore via satellite (data are available at www.whoi.edu/itp). Water column measurements have a vertical resolution of about 25 cm and a horizontal resolution (profile spacing based on ice drift speed and frequency of profile returns) of a few kilometers along the drift track of the supporting ice floe. ITP 1 returned 4 one-way profiles per day. Only up-going profiles are used in the analysis because the ITP's CTD sensors are located at the top of the profiler so that they are affected by turbulence in the wake of the profiler body. This affects the measurement of fine-scale double-diffusive structures of interest here. Further details of the ITP system and processing procedures are given by Krishfield *et al.* [2008].

The total along-track drift (cumulative distance) of ITP 1 was about 3500 km (corresponding to a net displacement of about 1200 km) in the Beaufort Gyre region during the course of 1.5 years (16 August 2005 to 8 January 2007, Figure 1b). The general water-column structure (from the ice-ocean interface to 750 m depth) in this region is as follows: a surface mixed layer ~ 20 m deep; a warmer Pacific Summer Water layer [e.g., Timmermans *et al.*, 2014] centered around 75 m depth; a cooler Pacific Winter Water layer [e.g., Jones *et al.*, 1995] centered around 150 m depth; a relatively warm and salty AW layer, which has a maximum temperature at around 400 m depth. A well-defined DC staircase is present in the upper part of this AW layer (~ 250 m depth, Figures 1a and 1c). Typical jumps between consecutive mixed layers (a few to several meters thick) within the DC staircase are $\sim 0.04^\circ\text{C}$ and ~ 0.014 for potential temperature and salinity, respectively. Interface thicknesses are ~ 10 cm based on microstructure measurements reported by Timmermans *et al.* [2008a]. Underlying the DC staircase is a series of intrusive layers (centered near 400 m) that is characterized by a region of weaker background stratification (in both temperature and salinity) and thicker apparently mixed layers than those in the overlying staircase (Figure 1). Each of these layers is actually the weak-gradient SF staircase component of a thermohaline intrusion.

3. Characterization of the Atlantic Water Eddy

On 2 September 2005, ITP 1 drifted into anomalously warm AW and appears to have sampled the edge of a warm-core anticyclonic eddy centered at depths corresponding to the AW temperature maximum. Around 20 days later, at a distance of ~ 18 km to the northeast of the initial encounter, the ITP sampled anomalously warm AW and convex isopycnal displacements bounding the warm core in depth. On the assumption that both encounters were of the same AW eddy (appropriate given the low frequency of AW eddies in this region [see e.g., Carpenter and Timmermans, 2012]), one may estimate the eddy translation velocity to be around 0.01 m s^{-1} in a northeast direction, assuming a direct path between encounter locations. The inferred direction of eddy propagation is consistent with the large-scale Beaufort Gyre circulation in this region [Proshutinsky *et al.*, 2009]. This estimate of eddy translation speed is nearly 1 order of magnitude smaller than the mean ITP drift speed averaged over the duration between the first and second encounters, which we infer from GPS measurements to be $\sim 0.07 \pm 0.04\text{ m s}^{-1}$. Thus, the ITP measurements may be viewed approximately as a synoptic sampling of a stationary eddy.

We focus only on the second encounter of the AW eddy by the ITP as there were many more profiles for analysis. We use 34 up-going profiles that were made during 17 days (15 September 2005 to 2 October 2005) over an along-track distance of about 85 km (in the vicinity of the red dot, Figure 1b). Time-depth transects of potential temperature, salinity, and density (Figures 2a and 2b) show divergence of isopycnals around a depth of 280 m associated with the anticyclone in the depth range between about 150 m and the maximum sampled depth (750 m). It is simplest to examine the lateral temperature-salinity structure across the eddy by considering a transect from the ambient water to the eddy core (e.g., point A to point C, Figures 2a and 2b). In the top half of the eddy, following isopycnal layers from point A to point C (the layers between around 300 and 450 m depth at point C), temperature and salinity both increase from the ambient water to the core. That is, the warm core of the eddy is compensated in density by the corresponding increase in salinity. Below this depth, along the isopycnal that is around 500 m depth through the SF staircase in the core of the eddy, salinity decreases from the ambient water (A) to the core (C), with a compensating cooling. Hence, the temperature and salinity structure is somewhat more complicated than a simple warm-core eddy. As the temperature and salinity of the eddy evolve, we anticipate that the warm core loses

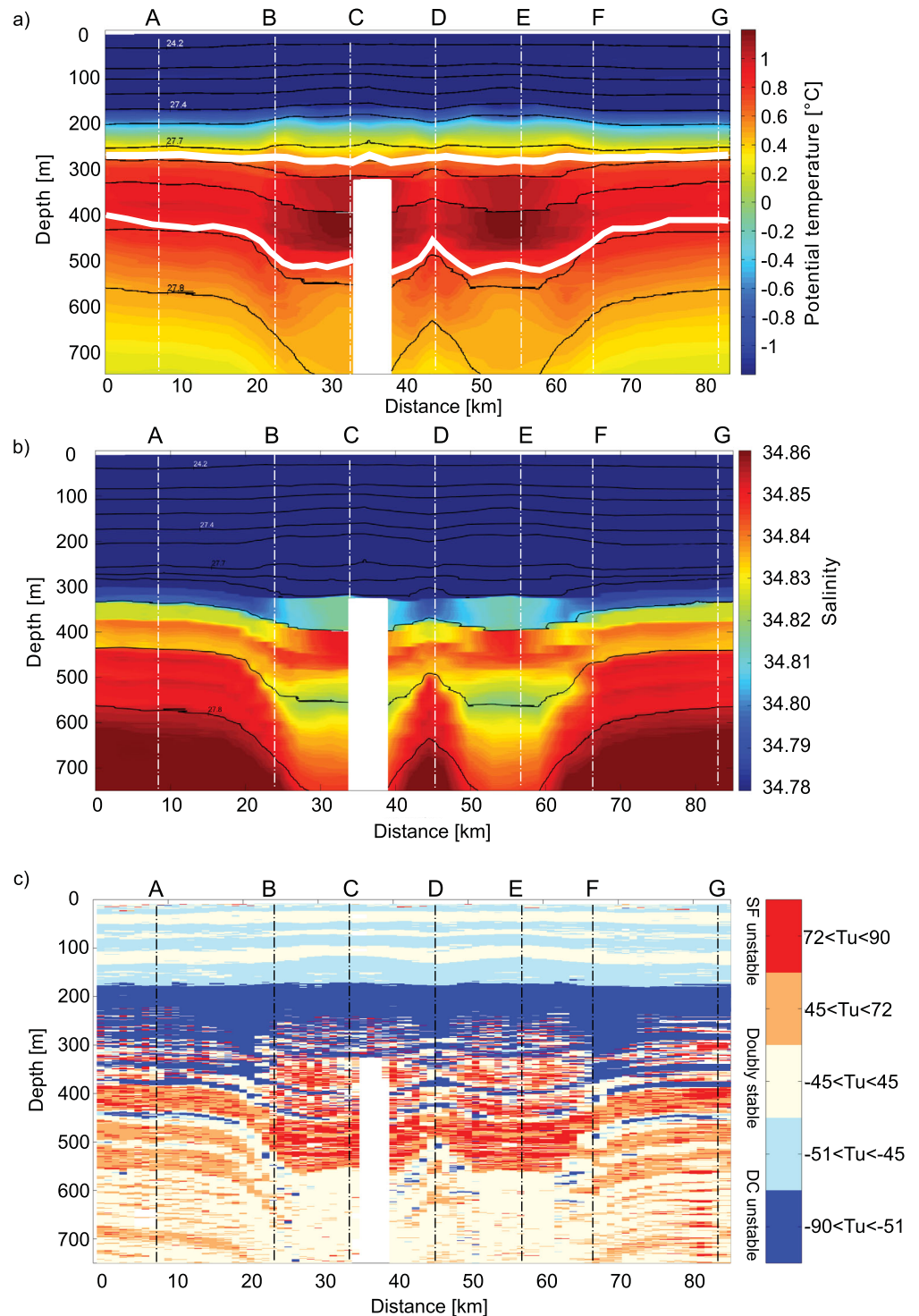


Figure 2. (a) Potential temperature ($^{\circ}\text{C}$) along the ITP drift track shown by the white dashed line in Figure 3a (corresponding letters A to G are indicated). Black contours are isopycnals (potential density anomaly relative to zero pressure, kg/m^3). Two white contours show isopycnals $\sigma_1 = 27.65 \text{ kg}/\text{m}^3$ and $\sigma_2 = 27.79 \text{ kg}/\text{m}^3$, considered for the analysis in section 5. (b) Salinity along the same transect with the lower color bar limit of 34.78 (i.e., smaller values of salinity are represented by the same color (dark blue), which is necessary to delineate the small changes in salinity in the eddy). (c) The Turner angle through the eddy with colors indicating DC unstable, SF unstable, and doubly stable regions (see text).

heat and salt to the overlying and underlying layers, ultimately modifying the vertical temperature and salinity gradients.

Eddy core properties provide a clue as to its probable formation location. The warmest eddy core water is $\sim 0.3^\circ\text{C}$ warmer than the maximum potential temperature of the surrounding water ($\sim 0.95^\circ\text{C}$ at around 400 m). This eddy was likely formed due to instability of the AW boundary current [see e.g., Woodgate *et al.*, 2001]. Potential temperature in the boundary current in the vicinity of the Northwind Ridge in 2005 was $\sim 1^\circ\text{C}$ [McLaughlin *et al.*, 2009], somewhat cooler than the $\sim 1.3^\circ\text{C}$ eddy core. Further upstream, in the vicinity of the Lomonosov Ridge, however, core temperatures of the AW boundary current are comparable to eddy core temperatures [Polyakov *et al.*, 2011]. Given the spatial and temporal variability in AW boundary current structure [e.g., Woodgate *et al.*, 2007], we speculate that the eddy was formed by baroclinic instability somewhere in the general region between the Lomonosov and northern Northwind Ridges.

Near the core of the AW eddy, thermohaline intrusions are more pronounced than in the surrounding (ambient) water, i.e., stronger temperature and salinity gradients between thicker intrusive layers (Figure 1c). The DC staircase in the upper part of the eddy shows no major differences from that in the ambient water, except at the eddy flanks where a well-defined staircase structure is absent. An SF staircase appears only at the base of the AW eddy, where temperature-salinity stratification differs appreciably from that of the ambient water in the same depth range. Close inspection indicates that the salinity profile through the eddy core is destabilizing where the SF staircase is present. The most pronounced SF staircase is observed immediately below the center of the eddy ~ 550 m depth (Figure 1c). The typical interface thickness for the SF steps is ~ 1 m (resolved by the ITP with vertical resolution of about 25 cm), and temperature and salinity interface jumps are $\sim 0.06^\circ\text{C}$ and ~ 0.002 respectively. A well-defined SF staircase is absent at the flanks of the eddy and in the ambient water.

Eddy azimuthal velocity can be estimated from dynamic heights assuming cyclogeostrophic balance and a level-of-no-motion in the integration of 750 m depth. The 750 m depth limitation of the ITP profiles may contribute some error in the velocity magnitude if there is nonnegligible velocity below this. For example, a level of no motion of 650 m depth yields a smaller cyclogeostrophic velocity by about 20%, although qualitatively the velocity profile remains the same. Note that the velocity estimates are only a lower bound given the finite horizontal profile spacing (on average ~ 2 km for the profiles analyzed here).

For the computation of cyclogeostrophic velocity, the eddy center position must be known [see e.g., Padman *et al.*, 1990]. To estimate the eddy center position and its radius, we assume a form for its velocity structure and minimize the error between the velocity obtained using an idealized eddy structure and cyclogeostrophic velocity computed from the measurements. A Rankine vortex structure is consistent with past observations of mesoscale eddies [e.g., Flór, 2010] including Arctic Ocean eddies [e.g., Timmermans *et al.*, 2008b; Zhao *et al.*, 2014], and has a velocity field given by

$$V(r) = \begin{cases} \frac{V_{\max} r}{R} & r < R \\ \frac{V_{\max} R}{r} & r > R, \end{cases} \quad (1)$$

where V_{\max} is maximum azimuthal velocity, R is eddy radius, and r is distance from the eddy center. The non-linear regression procedure involves a best guess of the eddy center location (latitude and longitude), and computation of cyclogeostrophic velocity from this center on a depth level of 300 m (the level of maximum cyclogeostrophic velocity). Azimuthal velocity is then computed from (1), adjusting V_{\max} and R to minimize the difference (using the method of least squares) from cyclogeostrophic velocity for the chosen eddy center location. This procedure is repeated for all possible eddy center locations to converge on the best combination of R , V_{\max} , and eddy-center location. This fitting yields an eddy radius of $R = 9 \pm 1$ km, consistent in magnitude to the first baroclinic Rossby deformation radius in this region [Zhao *et al.*, 2014]. The lower bound of maximum azimuthal velocity on 300 m depth is $V_{\max} = 0.13 \pm 0.01 \text{ m s}^{-1}$ (Figure 3). These values give a Rossby number ($Ro = 2V_{\max}/fR$, where $f = 1.4 \times 10^{-4} \text{ s}^{-1}$ is the Coriolis parameter) [see Zhao *et al.*, 2014] of $Ro \approx 0.2$.

A Gaussian model [e.g., von Appen *et al.*, 2014], $V = V_{\max}(r/R)\exp\left[\frac{1}{2}(1-(r/R)^2)\right]$, which has a smooth velocity profile and continuous first derivative, is also a reasonable approximation of the velocity structure, and the

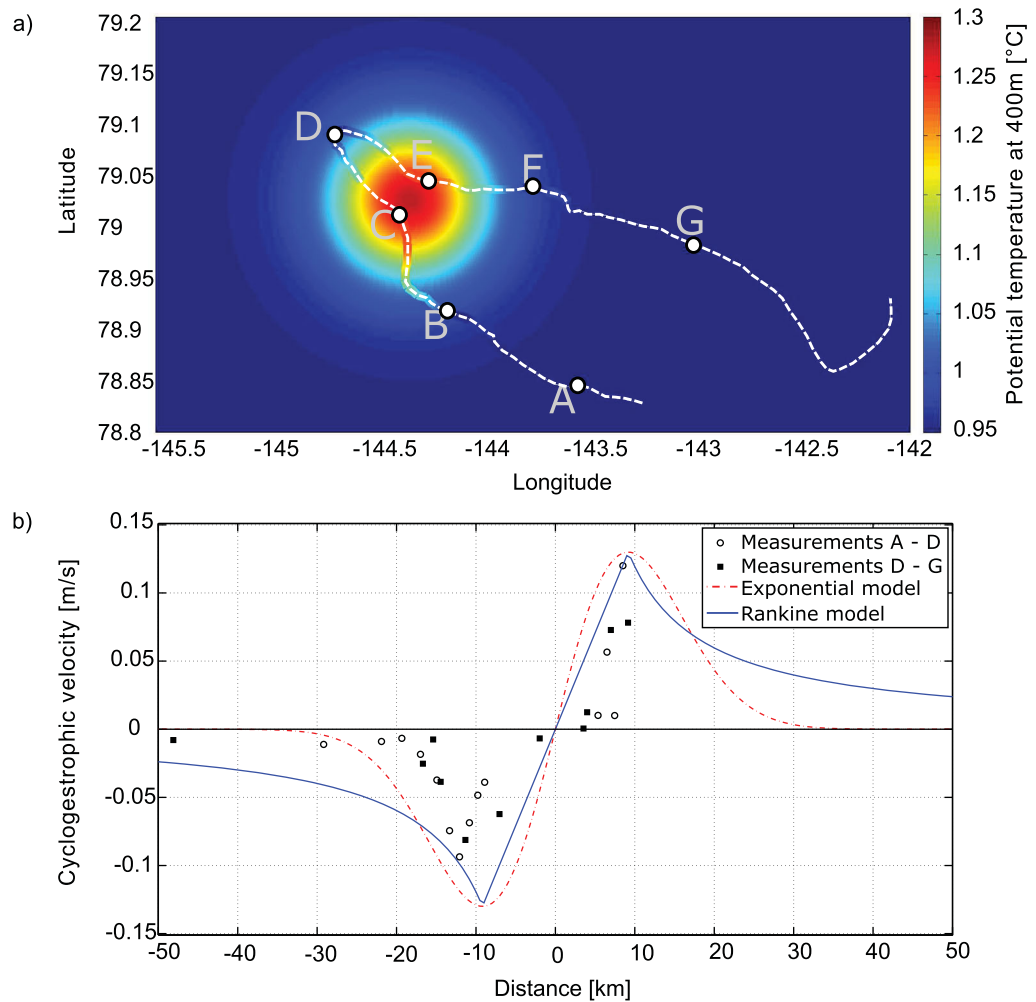


Figure 3. (a) Map showing the ITP drift track through the eddy (the dashed white line with colors representing potential temperature ($^{\circ}\text{C}$) at 400 m depth) and the reconstructed potential temperature field computed using a Gaussian distribution $\theta = \theta_0 + \Delta\theta \exp[-r^2/(2\delta R^2)]$, where θ_0 is ambient water potential temperature (at 400 m), $\Delta\theta = \theta_0 - \theta_a$ is the difference between the eddy core potential temperature (θ_0) and the ambient water potential temperature, and δ is a nondimensional shape parameter that is part of the fit. The eddy radius $R = 9 \pm 1$ km and core position are used from the velocity fit as described in the text. Regression results give $\delta = 0.60 \pm 0.06$, $\Delta\theta = 0.3^{\circ}\text{C}$, and core potential temperature $\theta_0 = 1.3 \pm 0.1^{\circ}\text{C}$. (b) Cyclogeostrophic velocity (m/s) at 300 m depth along the ITP drift track shown in Figure 3a. Zero distance corresponds to the core position of the eddy estimated from the least squares fit (see text). Negative velocities represent negative radii, and positive velocities represent positive radii. The solid blue line represents the Rankine vortex model (1) and the dashed red line is the Gaussian model. The data do not extend beyond 10 km on the positive side of the x axis because the ITP drift track is a U-turn at point D; the ITP transected the eddy twice: first, going to the northwest and then back through the eddy in a southeast direction.

choice of fit makes little difference to the characterization of the eddy (Figure 3). A Gaussian model seems to better represent the potential temperature θ field; a good fit of measured values to an empirical Gaussian temperature distribution can be obtained (assuming the core position and radius computed above) on a depth level of 400 m, where the maximum potential temperature of the AW eddy was sampled (Figure 3).

4. Double-Diffusive Structures Within the Eddy

In order to examine the impact of velocity shear on double diffusion, we begin by characterizing the range of double-diffusive structures within and around the eddy. The condition for double-diffusive instability can be characterized in terms of the vertical density ratio $\overline{R}_\rho = \beta \overline{S}_z / \alpha \overline{\theta}_z$, where θ_z and S_z are vertical gradients of potential temperature and salinity, and the overbar represents a bulk gradient as opposed to a temperature or salinity gradient across a single interface, $\alpha = -(1/\rho_0)(\partial\rho/\partial\theta)_{S,p}$ is the thermal expansion coefficient, $\beta = (1/\rho_0)(\partial\rho/\partial S)_{\theta,p}$ is the saline contraction coefficient, and ρ_0 is a reference density. Double-diffusive

instability can occur when either both potential temperature and salinity increase with depth (the DC type of double diffusion, $\overline{R}_\rho > 1$) or both quantities decrease with depth (the SF type of double diffusion, $1/\overline{R}_\rho > 1$; note that in the SF case, the density ratio is often defined as the inverse of the definition for \overline{R}_ρ used here). In general, $\overline{R}_\rho < 10$, where DC staircases are found [e.g., Kelley et al., 2003], while for an SF-unstable stratification, $1/\overline{R}_\rho < 2$, where staircases are observed (see Radko [2013], for a summary of these observational studies).

An alternative indicator of the stability of a water column to double-diffusive processes is the Turner angle, \overline{Tu} [Ruddick, 1983]. \overline{Tu} is defined as a function of the vertical density ratio

$$\overline{Tu} = \tan^{-1} \left(\frac{1 + \overline{R}_\rho}{1 - \overline{R}_\rho} \right), \quad (2)$$

and avoids the issues of the infinite ranges and ambiguous sign of \overline{R}_ρ (i.e., $\overline{R}_\rho < 0$ could mean either doubly stable or unstable stratification). When \overline{Tu} is in the range $[-90^\circ : -45^\circ]$ the water column is DC unstable, while strong DC instability is characterized by $-90^\circ < \overline{Tu} < -51^\circ$ ($\overline{Tu} = -51^\circ$ corresponds to $\overline{R}_\rho = 10$), and weak DC instability by $-51^\circ < \overline{Tu} < -45^\circ$. For \overline{Tu} within $[45^\circ : 90^\circ]$, stratification is susceptible to SF, where strong SF instability is characterized by $72^\circ < \overline{Tu} < 90^\circ$, and weak SF instability by $45^\circ < \overline{Tu} < 72^\circ$ [Ruddick, 1983]. \overline{Tu} in the range $[-45^\circ : 45^\circ]$ indicates a doubly stable region. For $|\overline{Tu}| > 90^\circ$, the water column is gravitationally unstable.

The AW eddy shows the complete spectrum of double-diffusive instabilities from DC unstable regions at its top boundary to the SF instability at its base, with thermohaline intrusions in between (Figure 2c). \overline{Tu} is computed through the eddy by averaging potential temperature and salinity gradients over 1.5 m above 325 m depth where ~ 1 m DC layers are present. Below 325 m depth where intrusions are present, and an SF staircase underlies the intrusions in some profiles, \overline{Tu} is computed by averaging gradients over 5 m. Depth segments over which to average were chosen as a trade-off between the necessity for fine vertical resolution and elimination of noise in the profiles.

Several distinct \overline{Tu} zones are clearly identified (Figure 2c). The upper layers (shallower than 200 m) show regular alternating bands of doubly stable and weak DC stratification. This banding indicates different water layers: a shallow near-surface temperature maximum associated with solar absorption during summer [e.g., Jackson et al., 2011] overlies layers of Pacific Ocean origin modified over all seasons. Close inspection in depth ranges with weak DC-favorable \overline{Tu} values indicates hints of poorly defined staircase structures, with mixed layer thicknesses of ~ 1 –2 m. The depth interval between 190 and 325 m shows almost exclusively \overline{Tu} in the range $[-90^\circ : -51^\circ]$, indicating strong DC instability. Between 325 and 500 m depth in the ambient water (zones A and G, Figure 2c) is characterized by thermohaline intrusions, and \overline{Tu} alternating in depth between DC and SF regimes. Thermohaline intrusions are also evident in \overline{Tu} values in the core of the eddy, and appear to be laterally coherent from the ambient water to the core. The depth interval between 450 and 550 m at the base of the eddy (zones C and E, Figure 2c) is strongly SF-unstable, and marked by a pronounced SF staircase that is not present in the ambient water. Depths below ~ 500 m in the ambient water and below ~ 550 m at the location of the eddy are generally doubly stable. However, \overline{Tu} values indicate layers prone to weak SF instability and small layers of ~ 1 –2 m thickness appear in some profiles.

5. Double Diffusion in the Presence of Shear

Past studies have addressed the question of what may cause the destruction or disappearance of staircase structures and the relative roles of turbulent and double-diffusive mixing. In the Arctic setting, it has been suggested that the absence of DC staircase structures could be due either to large values of \overline{R}_ρ (implying weak double-diffusive fluxes) or enhanced shear-driven turbulent mixing in the boundary regions [e.g., Timmermans et al., 2003, 2008a]. To assess the stability properties of the water column influenced by the shear associated with the eddy, we use the geostrophic Richardson number, where the shear S_g (the vertical gradient of the horizontal velocity) is computed by the thermal wind balance [see e.g., van Gastel and Pelegrí, 2004]. That is,

$$Ri_g = \frac{N^2}{S_g^2}, \quad (3)$$

where $N^2 = -(g/\rho_0)(\partial\rho/\partial z)$ is the buoyancy frequency, $S_g = \left(\frac{g}{\rho_0 f}\right)(\partial\rho/\partial x)$, g is gravitational acceleration, and x is distance along the ITP drift track between profiles. Note that only the geostrophic shear is

considered here (and not the cyclogeostrophic shear). For this $Ro \approx 0.2$ anticyclone, the magnitude of cyclogeostrophic shear is larger by only several percent.

To quantify the presence or absence of a staircase (or step structure), we introduce a step index parameter. This parameter is computed over a depth interval centered on an isopycnal that remains in a given staircase zone laterally from the ambient water through the core of the eddy, at the top of the eddy for the DC regime (shallow white contour, Figure 2a) and at the base of the eddy for the SF regime (deep white contour, Figure 2a). The step index is calculated to be the number of layers over a given depth. Each step is detected based on two consecutive peaks in vertical potential temperature gradient (θ_z) that correspond to sharp interfaces between the mixed layers, where $\theta_z > 0.03^\circ\text{C}/\text{m}$ is found to be an appropriate threshold for interface detection. The step index for a DC staircase is computed within a 30 m depth interval (± 15 m) around the chosen isopycnal (at depths of the DC staircase, 30 m is about the largest depth interval where property gradients can be approximated to be linear, and this is required for computation of bulk properties). The step index for an SF staircase is computed within a 60 m depth interval (± 30 m) around a chosen isopycnal. The larger depth interval for the SF regime encompasses the entire vertical extent of the SF staircase. Visual inspection of the profiles confirms that low step indices are consistently associated with the absence of a well-defined step structure and high step indices are consistently associated with a robust staircase. For more general application, the step index as defined here should be used with caution because higher step indices may be not only associated with the presence of layers, but possibly also thinner layers; in our case, this is not an issue because step thicknesses do not change appreciably over the region and depth ranges considered.

We examine the vertical structure of the water column by evaluating the following gradient quantities: the absolute value of geostrophic shear $\overline{S_g}$, density ratio $\overline{R_\rho}$, buoyancy frequency $\overline{N^2}$, and the geostrophic Richardson number $\overline{Ri_g}$. Each of these is based on salinity, potential temperature, and potential density (referenced to the surface) averaged over the same depth interval used for the step index calculations, i.e., 30 m for the DC case and 60 m for the SF case (see Figures 4 and 5, respectively). Such averaging gives the bulk characteristics rather than the properties of individual interfaces within staircase structures.

5.1. The DC Regime

At the top of the eddy, we choose the $\sigma_1 = 27.65 \text{ kg/m}^3$ isopycnal (shallow white contour, Figure 2a) for analysis because geostrophic shear is largest in a 30 m depth range centered around this isopycnal at the eddy flanks, and is minimal close to the eddy center. Visual inspection of potential temperature profiles in the depth range centered on σ_1 indicates that the DC-type staircase is present within the eddy core (i.e., closest to the horizontal eddy center) and away from the eddy (in the ambient water) where shear is weak or absent (Figure 4a).

The vertical density ratio is $\overline{R_\rho} \approx 4$ in the ambient water, in agreement with typical values of vertical density ratio in this region [Timmermans *et al.*, 2008a]. $\overline{R_\rho}$ remains within the DC-favorable range even at the eddy flanks (locations B, D, and F, Figures 3a and 4) where steps are not observed and $\overline{Ri_g}$ is relatively small. Within the eddy core (C and E, Figure 4), $\overline{R_\rho}$ decreases slightly, indicating somewhat stronger susceptibility to the DC type of double diffusion, although across the eddy, $\overline{R_\rho}$ remains within the DC-favorable range ($\overline{R_\rho} \approx 3.5$).

The buoyancy frequency $\overline{N^2}$ is minimum within the weakly stratified eddy core, being about half the value it attains in the ambient water. The geostrophic Richardson number is highest in zones of low shear outside the eddy and within the eddy core, and attains values $\overline{Ri_g} \sim O(100)$ at the eddy flanks (B, D, and F, Figure 4). There is a strong correlation between step index and the magnitude of the geostrophic shear (Figure 6a), with large step index (indicating a robust DC staircase) both in the ambient water and within the eddy core (A, C, E, and G, Figure 4) and low step index on the flanks of the eddy (where azimuthal speeds and vertical shear are maximal; B, D, and F, Figure 4). Small values of step index where shear is low (Figure 6a) are generally observed just outside the eddy where computed shear is weak while steps are not robust (16–19 km and around 70 km, Figure 4b); given the limitations of the geostrophic velocity calculations discussed earlier, velocity measurements are required to analyze this further. The geostrophic Richardson number below which the step index decreases by $1/e$ is computed from an empirical fit (Figure 6a), using the mean value of $\overline{N^2} \approx 2 \times 10^{-5} \text{ s}^{-2}$ in regions where $\overline{S_g}$ is around $2 \times 10^{-4} \text{ s}^{-1}$, to be $\overline{Ri_g} \sim O(100)$. We perform the fit on $\overline{S_g}$ because $\overline{Ri_g}$ varies by several orders of magnitude across the eddy.

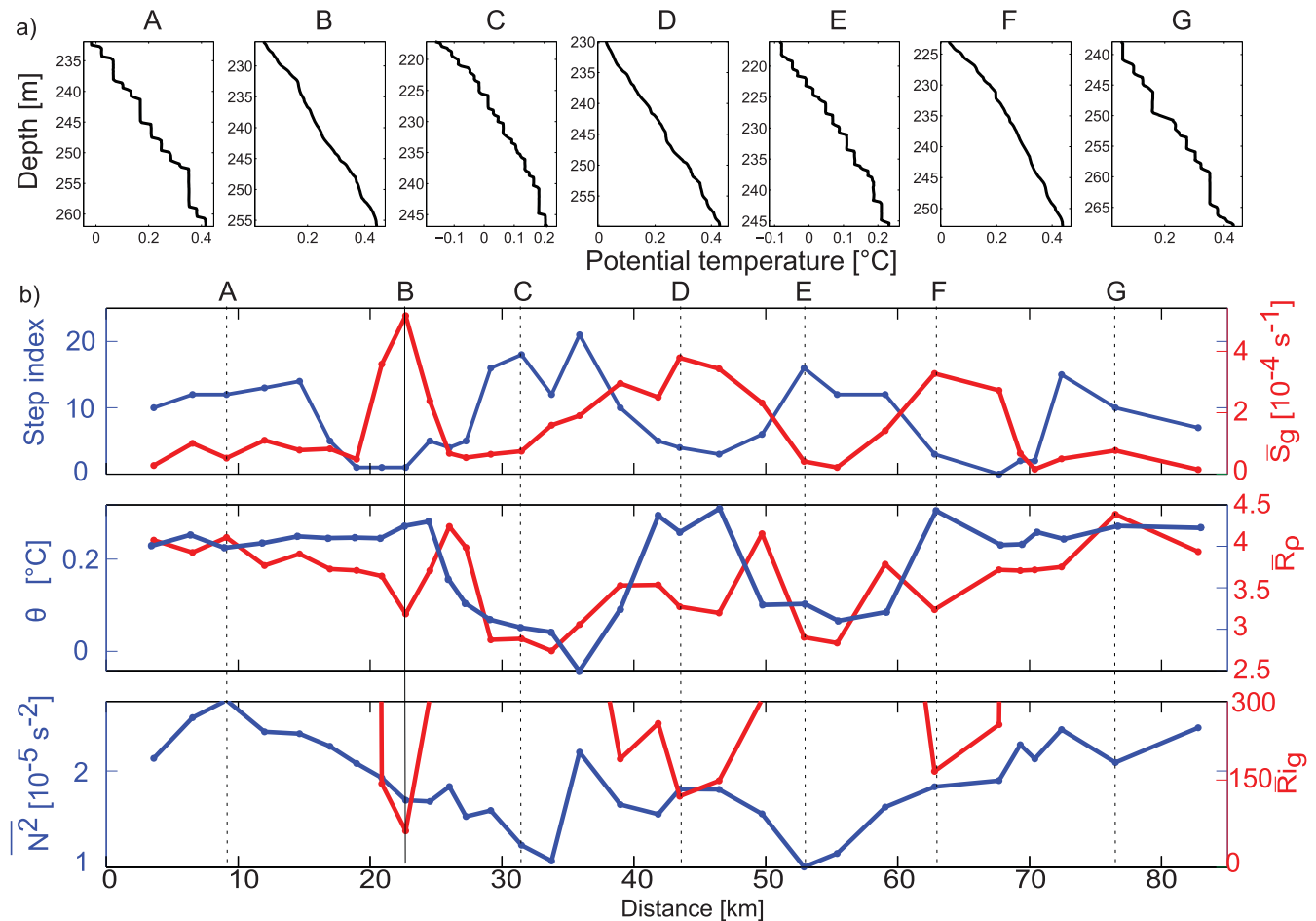


Figure 4. (a) Representative potential temperature profiles at locations corresponding to the letters shown in Figure 3a. The depth ranges shown correspond to the 30 m depth interval centered around σ_1 (i.e., the top white contour in Figure 2a) at each of the locations shown. (b) The DC step index, absolute value of \bar{S}_g (s^{-1}), potential temperature θ ($^{\circ}C$), density ratio \bar{R}_ρ , buoyancy frequency \bar{N}^2 (s^{-2}), and Richardson number \bar{Ri}_g evaluated over the 30 m depth range centered on σ_1 .

5.2. The SF Regime

To investigate the SF regime at the eddy base, we choose an isopycnal that spans the SF staircase, $\sigma_2 = 27.79 \text{ kg/m}^3$ (deep white contour, Figure 2a). Steps are absent at the eddy flanks (B, D, and F, Figure 5a) and in the ambient water (A and G, Figure 5a) where temperature-salinity stratification is not susceptible to SF-staircase formation. Below the eddy center, temperature and salinity decreases with depth providing conditions amenable to an SF staircase with $\bar{1}/\bar{R}_\rho \sim 2$. Near the beginning and end of the transect (around 5 and 75 km, Figure 5), σ_2 lies within the double-diffusive intrusions in the ambient water (where both DC and SF unstable gradients exist) and averaging over the considered depth range gives low values of $\bar{1}/\bar{R}_\rho$. There is some evidence in the ambient waters for the presence of an SF staircase, with the occurrence of a few thin mixed layers in some profiles. This lateral change in structure is an important feature (and the subject of a future study) that relates to the unresolved issue of staircase formation; a double-diffusive staircase is thought to form either by thermohaline intrusions evolving into a staircase [Merryfield, 2000], or instability of a vertical profile and subsequent layer merging [Radko, 2003], or both.

The step index is zero in the ambient water (A and G, Figure 5) where temperature-salinity stratification is not susceptible to SF-staircase formation. The step index is also zero where shear is high (B, D, and F, Figure 5), even though the temperature-salinity stratification is SF-unstable; following σ_2 from the ambient water into the eddy, $\bar{1}/\bar{R}_\rho$ changes from doubly stable to SF-unstable. As shear decreases from the flanks to the eddy center, the step index increases (C and E, Figure 5).

In summary, there are three distinct regions across the lower portion of the eddy: low shear and low step index characterizing the ambient water, low shear and high step index characterizing the eddy core, and a

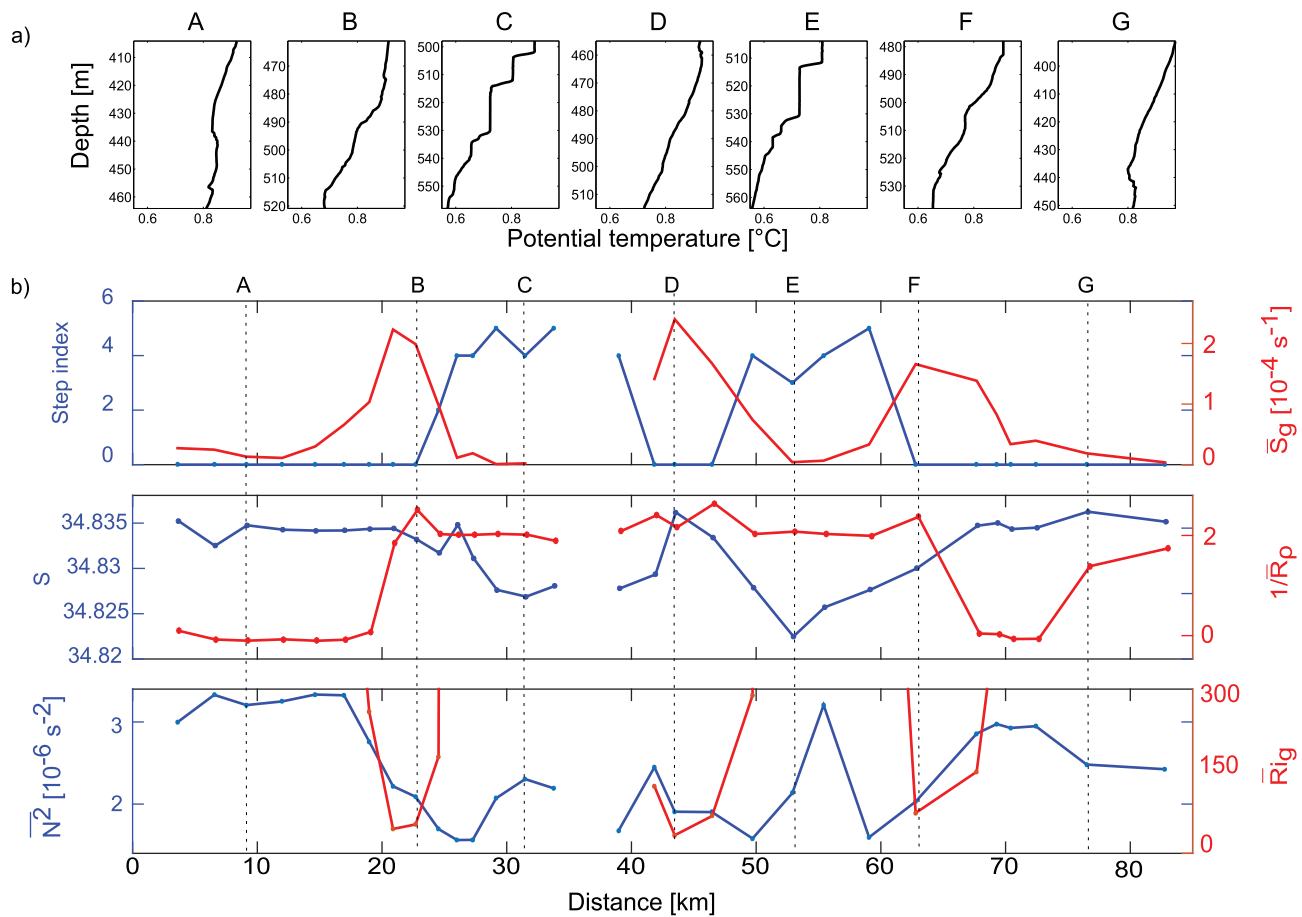


Figure 5. (a) Representative potential temperature profiles at locations corresponding to the letters shown in Figure 3a. The depth ranges shown correspond to the 60 m depth interval centered around σ_2 (i.e., the bottom white contour in Figure 2a) at each of the locations shown. (b) The SF step index, absolute value of shear \bar{S}_g (s^{-1}), salinity S , inverse density ratio $1/\bar{R}_\rho$, buoyancy frequency \bar{N}^2 (s^{-2}), and Richardson number \bar{Ri}_g across the eddy evaluated over the 60 m depth range centered on σ_2 .

transition zone at the eddy flanks (Figure 6b). The Richardson number is high outside the eddy and within the eddy core, where shear is small. While these depths are less stratified than at the top of the eddy, the magnitude of shear is smaller at these depths, and $\bar{Ri}_g \sim \text{O}(100)$ in the eddy flank regions (comparable to the value in the flank regions at the top of the eddy). The geostrophic Richardson number below which the step index decreases by $1/e$ is again computed from an empirical fit to \bar{S}_g (Figure 6b), using the mean value of $\bar{N}^2 \approx 10^{-6} \text{ s}^{-2}$ in regions where \bar{S}_g is around $0.5 \times 10^{-4} \text{ s}^{-1}$, to be $\bar{Ri}_g \sim \text{O}(100)$. We discuss this further in section 7.

6. Implications for Mixing and Eddy Evolution

While we have shown that double-diffusive staircases do not persist at the flanks of the eddy, the consequences for heat, salt, and buoyancy fluxes in and around the eddy remain to be examined. The direction of the vertical buoyancy flux differs between purely turbulent mixing and purely double-diffusive: shear-driven turbulence mixes density down-gradient, whereas double diffusion (both DC and SF) mixes density up-gradient (i.e., the flux of density is downward and stratification increases) as double diffusion is driven by the release of potential energy in the unstable component. Previous investigators have suggested that the occurrence of turbulence in double-diffusively favorable conditions leads to a net buoyancy flux that depends upon the relative strength of each type of mixing [e.g., *St. Laurent and Schmitt, 1999*]. When a double-diffusive staircase is not observed, it is likely that the up-gradient density flux is not sufficient to maintain layers. However, the absence of a well-formed staircase does not necessarily mean that double-diffusive mixing is not taking place; it is possible that both double-diffusive mixing and turbulent mixing operate concurrently.

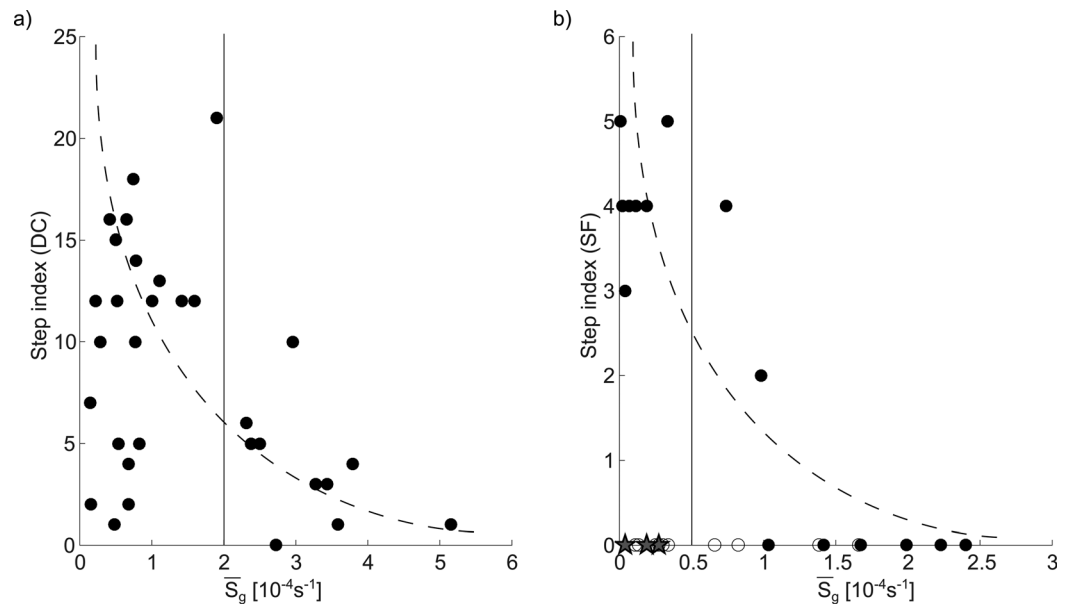


Figure 6. Dependence of shear on step index for (a) the top (DC region) of the eddy, where for all points ($-90^\circ < \overline{T\bar{u}} < -45^\circ$) (DC favorable); (b) the bottom (SF region) of the eddy, where open circles indicate $\overline{T\bar{u}}$ in the range $[-45^\circ : 45^\circ]$ (doubly stable), black closed circles indicate ($45^\circ < \overline{T\bar{u}} < 90^\circ$) (SF favorable), and stars are values at the start and end of the transect where ($45^\circ < \overline{T\bar{u}} < 90^\circ$), although steps are not observed (see text). The vertical solid line indicates the value of shear where the step index is $1/e$ of its value for no shear. The dashed line is an empirical fit (considering only the closed black circles in Figures 6b).

In order to quantify the double-diffusive and turbulent contributions to the total mixing, microstructure measurements are needed to estimate the rate of dissipation of kinetic energy ϵ , and to infer the mixing efficiency (or dissipation flux coefficient) based on this [see e.g., Thorpe, 2005]. A three-parameter family (mixing efficiency, vertical density ratio and either the Richardson number or the buoyancy Reynolds number to quantify turbulence) allows for the delineation of double-diffusive and turbulent mixing [e.g., St. Laurent and Schmitt, 1999; Inoue et al., 2007]. Through examination of the statistical distribution of microstructure measurements to determine the relative contribution of turbulent and double-diffusive mixing in a given setting, effective diffusivity can be estimated as a weighted sum of these two types of mixing [e.g., St. Laurent and Schmitt, 1999].

Without microstructure measurements, it is not possible to determine how total mixing is partitioned between double-diffusive and turbulent contributions at the eddy flanks. However, we can constrain diffusivity estimates by assuming that shear-driven turbulence dominates at the eddy flanks, and that pure double diffusion takes place in regions with a well-defined staircase. In this way, we can examine how lateral (radial) changes in vertical fluxes across the eddy may influence its temperature/salinity evolution and dynamics.

6.1. Turbulent Fluxes at the Eddy Flanks

To estimate turbulent heat, salt, and buoyancy fluxes in the flank regions, we first estimate turbulent diffusivities at the eddy flanks (assumed to be purely turbulent) at both the top and bottom of the eddy. With knowledge of the diffusivities, the heat flux F_θ and the salt flux F_S can be estimated as

$$F_\theta = \rho c_p K_\theta \overline{\theta_z}, \quad (4)$$

$$F_S = K_S \overline{S_z}, \quad (5)$$

where c_p is the specific heat of seawater, and K_θ and K_S are heat and salt diffusivities ($K_\theta = K_S$ in the case of fully turbulent mixing, as assumed here for the eddy flanks).

In the absence of microstructure measurements, a turbulent diffusivity can be estimated by examining density overturns (i.e., unstable regions in the density profile). Such density inversions give the vertical scale of overturning eddies (turbulent mixing), or the Thorpe scale L_T defined as the root-mean-square of vertical

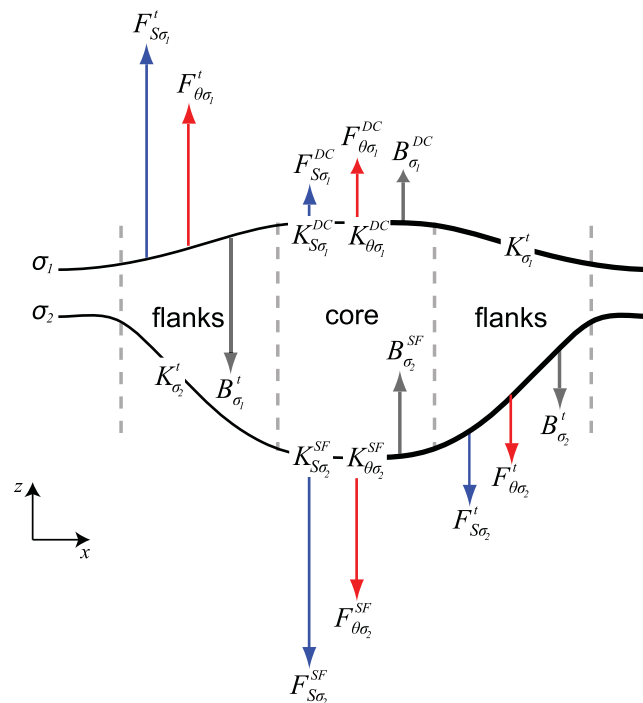


Figure 7. Schematic showing a time-depth transect through the eddy; black lines show isopycnals σ_1 and σ_2 . The directions (and approximate relative magnitudes, not to scale) of heat (F_θ), salt (F_S), and buoyancy (B) fluxes, as well as diffusivities, are shown; superscripts DC and SF represent top and bottom staircase regions where purely double-diffusive mixing is assumed to occur; superscript t indicates the purely turbulent eddy flanks (top and bottom). Vertical grey dashed lines mark the boundaries between the eddy core and flanks. Fluxes at the eddy flanks are indicated only on one side of the eddy in order to simplify the diagram.

the resulting Thorpe scales [see Galbraith and Kelley, 1996; Timmermans *et al.*, 2003]. Further, we computed run lengths (i.e., the number of adjacent measurements in depth where the density difference from the sorted profile has the same sign) for both the resorted profile with added noise, as well as the original profile; noise should result in short runs of alternating positive and negative displacements while Thorpe displacements should have longer run lengths [see Galbraith and Kelley, 1996]. In this case, the Thorpe scale computed from the profile with added noise is $L_{TN} \approx 60$ cm, with an RMS run length of about 2 (close to the theoretical limit) [Galbraith and Kelley, 1996]. For the measured profile, $L_T \approx 10$ cm, with an RMS run length of about 11. That is, run lengths of the profile are much larger than the short run lengths associated with noise, and we conclude that the observed displacements can be attributed to mixing.

The diffusivity $K_{\sigma_1}^t$ estimated from Thorpe overturns may be compared to a turbulent diffusivity $K^t = \Gamma \epsilon / \overline{N^2}$ [Osborn, 1980] computed from microstructure measurements in the AW thermocline in regions where there is no double-diffusive staircase [see Rippeth *et al.*, 2015]. We take the rate of dissipation of turbulent kinetic energy to be $\epsilon \approx 10^{-9}$ W kg $^{-1}$ in the AW thermocline in the Canada Basin [Rippeth *et al.*, 2015]. The low dissipation rate is close to the noise floor [Rippeth *et al.*, 2015; see also Robertson *et al.*, 1995], and can provide only an upper bound on diffusivities. Estimates of the dissipation flux coefficient Γ can differ substantially depending upon the physics of the flow field [Moum, 1996] and the stage of the evolving turbulence [Smyth *et al.*, 2001]. Γ has been shown to vary from about 1 to 2 at the initial stages of shear-driven turbulence (when Kelvin-Helmholtz billows grow) toward ~ 0.2 when turbulence is fully developed [see e.g., Smyth *et al.*, 2001; Peltier and Caulfield, 2003]. Here we assume fully developed turbulent mixing at the eddy flanks, where intermittency in the turbulence is not likely to be a significant factor, and take $\Gamma \approx 0.2$, in general agreement with past observational studies [e.g., Moum, 1996]. These values for ϵ and Γ yield a turbulent diffusivity $K_{\sigma_1}^t \approx 10^{-5}$ m 2 s $^{-1}$, in agreement with that obtained in our Thorpe scale analysis. Finally, we note that turbulence in a stratified water column can be characterized by the buoyancy Reynolds number $Re_b = \epsilon / (\nu \overline{N^2})$ which is about 40 in the turbulent eddy flanks (where we use $\epsilon \approx 10^{-9}$ W kg $^{-1}$, kinematic

displacements of water parcels required to convert an observed unstable density profile into one with stable stratification [see Thorpe, 2005]. A turbulent diffusivity can be estimated from the Thorpe scale and the buoyancy frequency as $K^t \approx 0.1 \overline{N} L_T^2$ [e.g., Dillon, 1982].

At the top of the eddy, we again consider a 30 m depth interval centered around σ_1 . Stratification in this region is sufficiently strong that instrument noise is much smaller than the density change over the depth interval. Following the procedure of Timmermans *et al.* [2003], we compute $L_T \approx 10$ cm at the eddy flanks in this depth interval, which gives a turbulent diffusivity $K_{\sigma_1}^t \approx 10^{-5}$ m 2 s $^{-1}$ equal for both heat and salt (all notation is defined in Figure 7). In these low turbulence environments, there exists the possibility that unstable displacements indicate instrument noise [see Johnson and Garrett, 2004]. To consider this possibility, we added random noise (having an RMS value equal to 1.2×10^{-3} kg m $^{-3}$) to the resorted potential density profile around σ_1 and computed the

viscosity $\nu = 1.8 \times 10^{-6} \text{ m}^2 \text{ s}^{-1}$, and $\overline{N^2} = 1.5 \times 10^{-5} \text{ s}^{-2}$). This is above the threshold for the transition from molecular to turbulent mixing ($Re_b \approx 7$), but below the transition to a fully energetic turbulent regime, $Re_b > 100$; these concepts are reviewed by Ivey *et al.* [2008] who also point out that estimating the turbulent diffusivity as $0.2\epsilon/\overline{N^2}$ is a valid approximation when Re_b is in the range $7 < Re_b < 100$.

Having estimated the turbulent diffusivity, we can now compute turbulent fluxes, from (4) and (5), at the top flanks of the eddy (for the remainder of the text, positive (negative) fluxes are directed upward (downward)). With $K_\theta = K_S = K_{\sigma_1}^t$, and $\overline{\theta}_z \approx 0.014^\circ\text{C/m}$ and $\overline{S}_z = 2 \times 10^{-3} \text{ m}^{-1}$ over a 30 m depth interval centered around σ_1 , we find the turbulent heat and salt fluxes to be $F_{\theta\sigma_1}^t \approx 0.6 \text{ W/m}^2$ and $F_{S\sigma_1}^t \approx 2 \times 10^{-8} \text{ m s}^{-1}$.

The buoyancy flux can be expressed as

$$B = g \left(\frac{\alpha F_\theta}{\rho c_p} - \beta F_S \right) = g \frac{\alpha F_\theta}{\rho c_p} (1 - R_F), \quad (6)$$

where $R_F = \rho c_p \beta F_S / \alpha F_\theta$ is the flux ratio, quantifying the density flux of salt (βF_S) to the density flux of heat (αF_θ). Using (4) and (5), it can be shown that $R_F = \overline{R}_\rho$ at the eddy flanks, where turbulent diffusivities for salt and heat are equal. Therefore, with $\overline{R}_\rho \approx 3.5$, the buoyancy flux at the flanks is $B_{\sigma_1}^t \approx -2.5g\alpha F_{\theta\sigma_1}^t / \rho c_p \approx -2.3 \times 10^{-10} \text{ m}^2 \text{ s}^{-3}$.

We also use the Thorpe scale approach to estimate the turbulent diffusivity at the eddy flanks at the base of the eddy. Stratification at the eddy base is an order of magnitude weaker than at the top of the eddy, and noise in the density profile affects the results here [see e.g., Johnson and Garrett, 2004]. However, assuming a tight relationship between temperature and salinity, potential temperature may be used to assess overturns and calculate the Thorpe scale. We consider a depth range of 30 m centered around σ_2 to avoid intrusions at the eddy flanks that enter for a larger depth range. The basic state temperature profile is always decreasing with depth in the considered depth range (i.e., any increase in temperature with depth is associated with turbulent mixing rather than a salinity-compensated double-diffusive structure). In the flank regions, we find $L_T \approx 20 \text{ cm}$, corresponding to $K_{\sigma_2}^t \approx 10^{-5} \text{ m}^2 \text{ s}^{-1}$. This value falls within the range of typical values of diffusivity (inferred from microstructure) for water masses around 400 m depth in the region $(0.3-2) \times 10^{-5} \text{ m}^2 \text{ s}^{-1}$ [Rainville and Winsor, 2008].

Again, we consider the possibility of instrument noise affecting the Thorpe calculations. The same procedure is applied to the potential temperature profile around σ_2 , with the random noise taken to have an RMS value of $9 \times 10^{-4} \text{ }^\circ\text{C}$ (i.e., near the instrument resolution). Here $L_{TN} \approx 60 \text{ cm}$, with an RMS run length of 2.5 (close to the theoretical limit), and $L_T \approx 20 \text{ cm}$ with an RMS run length of 43, much larger than the RMS run length of the resorted profile with added noise. Again we conclude that the unstable regions in the density profile are real Thorpe displacements due to turbulent mixing.

We use the estimated value of turbulent diffusivity at the bottom flanks of the eddy ($K_{\sigma_2}^t$) to compute heat, salt, and buoyancy fluxes there. The turbulent heat and salt fluxes computed from (4) and (5) are $F_{\theta\sigma_2}^t \approx -0.2 \text{ W/m}^2$ and $F_{S\sigma_2}^t \approx -2 \times 10^{-9} \text{ m s}^{-1}$, where $\overline{\theta}_z \approx -5 \times 10^{-3} \text{ }^\circ\text{C/m}$ and $\overline{S}_z \approx -2 \times 10^{-4} \text{ m}^{-1}$ are the bulk vertical potential temperature and salinity gradients over a 60 m depth interval centered around σ_2 . The buoyancy flux can be estimated from (6), with $1/R_F = 1/\overline{R}_\rho \approx 2$, as $B_{\sigma_2}^t \approx 0.5g\alpha F_{\theta\sigma_2}^t / \rho c_p \approx -1.8 \times 10^{-11} \text{ m}^2 \text{ s}^{-3}$. We next estimate double-diffusive fluxes at the eddy core for comparison to these turbulent fluxes at the eddy flanks.

6.2. Double-Diffusive Fluxes at the Eddy Core

Heat and salt fluxes through the double-diffusive staircases at the top and base of the eddy core can be computed using 4/3-flux parameterizations based on the potential temperature and salinity differences across an interface between two adjacent mixed layers. Using the estimated double-diffusive fluxes, effective diffusivities in the DC and SF staircases can be computed from (4) and (5).

The double-diffusive heat flux across interfaces in the DC staircase may be parameterized based on the formalism of Kelley [1990]:

$$F_\theta^{DC} = 0.0032 e^{4.8/R_\rho^{0.72}} \rho c_p \left(\frac{\alpha g \kappa}{Pr} \right)^{1/3} (\Delta\theta)^{4/3}, \quad (7)$$

where $\Delta\theta$ is the potential temperature jump across interfaces, $c_p = 3980 \text{ J/(kg}^\circ\text{C)}$ is the specific heat of seawater, $Pr = \nu/\kappa$ is the Prandtl number, $\nu = 1.8 \times 10^{-6} \text{ m}^2 \text{ s}^{-1}$ is the kinematic viscosity, and $\kappa = 1.4 \times 10^{-7} \text{ m}^2 \text{ s}^{-1}$ is the

molecular diffusivity of heat. This parameterization has been shown to be a reasonable approximation for heat fluxes through the DC staircase in this region of the Canada Basin [Timmermans *et al.*, 2008a]. Equation (7) yields a heat flux through the DC staircase in the eddy core region of $F_{\theta\sigma_1}^{DC} \approx 0.15 \text{ W/m}^2$ around σ_1 , in agreement with the magnitude of DC heat fluxes in the ambient water of the central Canada Basin region computed by Timmermans *et al.* [2008a].

The salt flux in the DC staircase where $\overline{R_\rho} \approx 3.5$ may be estimated using the flux ratio, which has been shown empirically to be $R_F \approx 0.15$ [Turner, 1965]. This yields a salt flux of $F_{S\sigma_1}^{DC} \approx 2 \times 10^{-10} \text{ m s}^{-1}$. The buoyancy flux computed using (6) is $B_{\sigma_1}^{DC} \approx 0.85g\alpha F_{\theta\sigma_1}^{DC} / \rho c_p \approx 1.8 \times 10^{-11} \text{ m}^2 \text{ s}^{-3}$, directed upward (i.e., stratification increases when purely double-diffusive mixing takes place).

Using the DC heat flux, an effective diffusivity for heat at the top of the eddy core may be computed from (4) as $K_{\theta\sigma_1}^{DC} \approx 2.6 \times 10^{-6} \text{ m}^2 \text{ s}^{-1}$ (where $\overline{\theta_z} \approx 0.014^\circ\text{C/m}$). This value is comparable to a diffusivity inferred from velocity measurements of $10^{-6} \text{ m}^2 \text{ s}^{-1}$ between 150 and 400 m depth in the staircase region of the ambient water [Guthrie *et al.*, 2013]. Similarly, using the DC salt flux $F_{S\sigma_1}^{DC}$ (equivalently, writing the ratio of salt to heat diffusivities as $R_F/\overline{R_\rho}$), we find an effective diffusivity for salt $K_{S\sigma_1}^{DC} = 1.1 \times 10^{-7} \text{ m}^2 \text{ s}^{-1}$.

To compute a heat flux through the SF staircase at the base of the eddy core, we use the double-diffusive salt-flux parameterization of Schmitt [1979] together with the definition of R_F , which gives:

$$F_{\theta}^{SF} = C \frac{\rho c_p}{R_F \alpha} (g\kappa)^{1/3} (\beta \Delta S)^{4/3}, \quad (8)$$

where ΔS is the salinity jump across an interface, and the coefficient $C = 0.05 + 0.3\overline{R_\rho}^{-3}$ is an empirical function of the density ratio [Schmitt, 1981]. Numerical and observational studies indicate that $R_F \approx 1/0.7$ for $1/\overline{R_\rho} \approx 2$ in the SF staircase (an overview of these studies can be found in Radko [2013]). This yields a heat flux $F_{\theta\sigma_2}^{SF} \approx -0.8 \text{ W/m}^2$, and a salt flux $F_{S\sigma_2}^{SF} \approx -2 \times 10^{-8} \text{ m s}^{-1}$, through the SF staircase at the eddy base. These fluxes imply effective diffusivities of heat $K_{\theta\sigma_2}^{SF} \approx 4 \times 10^{-5} \text{ m}^2 \text{ s}^{-1}$ (where $\overline{\theta_z} \approx -5 \times 10^{-3}^\circ\text{C/m}$) and salt $K_{S\sigma_2}^{SF} \approx 1.1 \times 10^{-4} \text{ m}^2 \text{ s}^{-1}$ (using $R_F \approx 1/0.7$, $1/\overline{R_\rho} = 2$).

The buoyancy flux in the SF staircase is $B_{\sigma_2}^{SF} \approx -0.43g\alpha F_{\theta\sigma_2}^{SF} / \rho c_p \approx 6.2 \times 10^{-11} \text{ m}^2 \text{ s}^{-3}$. Note that the SF buoyancy flux at the base of the eddy is about 4 times larger than the DC buoyancy flux at the top, commensurate with the study of the evolution of an eddy of Mediterranean origin [Hebert, 1988] where heat loss from the top is dominated by the salt loss at its base with respect to buoyancy (i.e., a net loss of buoyancy due to double-diffusive fluxes) [see also Dmitrenko *et al.*, 2008].

6.3. Comparison of Turbulent and Double-Diffusive Fluxes

Double-diffusive and turbulent fluxes compete in setting the evolution of the eddy. The buoyancy flux is directed upward (i.e., stratification increases) in both the DC and SF staircases. In the flank regions at the top and bottom of the eddy, the buoyancy flux is directed downward, driving a decrease in stratification. Under the simplest assumption of no lateral redistribution of buoyancy, and area weighting the vertical buoyancy fluxes (the area of a horizontal slice through the eddy can be divided into approximately 1/4 core region and 3/4 flank regions), we find a net buoyancy flux into the eddy (i.e., the eddy becomes less dense over time). However, the lateral redistribution of buoyancy is likely to be important. Buoyancy is removed from the top of the eddy core, and replaced by turbulent mixing at its flanks. The bottom part of the eddy becomes more buoyant over time (by SF fluxes) at the core, while buoyancy is removed at its flanks by turbulent mixing in the deeper portion (Figure 7).

Similarly, the net heat and salt fluxes are governed by the combination of double-diffusive and turbulent processes. At the top of the eddy, the turbulent heat flux in the flank regions is larger by a factor of ~ 4 than the heat flux through the DC staircase. At the base of the eddy, the turbulent heat flux is about 4 times smaller than the double-diffusive heat flux through the SF staircase; the strongest heat fluxes are at the top flanks of the eddy and at the base through the SF staircase. The turbulent salt flux at the top is about 100 times larger than the double-diffusive salt flux through the DC staircase. At the eddy base, the turbulent salt flux is about 10 times smaller than the SF salt flux; as for the heat fluxes, the strongest salt fluxes are at the top flanks of the eddy and at the base through the SF staircase. The net fluxes may be considered to estimate eddy decay time scales.

6.4. Eddy Decay Time Scales

Time scales for dissipation of the anomalous temperature/salinity properties associated with the eddy may be estimated considering net fluxes (turbulent and double diffusive) from the eddy. We approximate the eddy as a cylinder of height $H_\theta \approx 200$ m (the height over which most of the anomalously warm water is concentrated) having a temperature anomaly of $\sim 0.3^\circ\text{C}$ from its surroundings. The potential temperature evolves according to $d\theta/dt = F_\theta^{\text{net}} / (\rho c_p H_\theta)$, where $F_\theta^{\text{net}} \approx 0.84 \text{ W/m}^2$ is the net heat flux from the eddy (using the area weighting as above). This yields a time for decay of the temperature anomaly of about 9 years. Similarly, the salinity anomaly (~ 0.03) is dissipated according to $dS/dt = F_S^{\text{net}} / H_S$, where $H_S \approx 100$ m is the thickness of the eddy in which the salinity anomaly is concentrated. The net salt flux from the eddy $F_S^{\text{net}} \approx 2.15 \times 10^{-8} \text{ m s}^{-1}$ (area weighted for double-diffusive and turbulent contributions) yields a decay time scale of about 4 years.

These estimates are an upper bound given that divergences of vertical heat and salt fluxes across the eddy induce lateral fluxes that dissipate the anomalies; these are also related to lateral fluxes associated with double-diffusive intrusions. Following *Hebert et al.* [1990], we consider the finite volume of anomalous water in the eddy core region to estimate the time for eddy decay by lateral processes (i.e., lateral mixing of the anomalous eddy core water by exchanging thermohaline intrusions). Estimates of lateral diffusivities in intrusive regions differ widely. *Walsh and Carmack* [2003] solved the lateral diffusion equation bounded by Arctic observations in the same general region as our eddy to estimate a lateral diffusivity due to AW intrusions of $K_H \approx 50 \text{ m}^2 \text{ s}^{-1}$. Through repeat observations of a Mediterranean eddy with double-diffusive intrusions, *Hebert et al.* [1990] estimated a lateral diffusivity for the intrusions of about $5 \text{ m}^2 \text{ s}^{-1}$ assuming salt lost from the eddy was predominantly by lateral mixing. We consider this range of lateral diffusivities ($5\text{--}50 \text{ m}^2 \text{ s}^{-1}$), and take the horizontal salinity gradient from the (anomalously salty) eddy core to the flanks to be about 0.01 over 9 km (the radius of the eddy). This would lead to a depletion of the lateral salinity gradient in about 1–3 years.

7. Summary and Discussion

We have characterized the variety of double-diffusive structures in and around an AW eddy and investigated how the geostrophic shear associated with the eddy correlates with the staircase structures. For the DC regime at the top of the eddy core, the vertical density ratio (and \overline{Tu}) indicates that the profile is susceptible to the diffusive instability and a well-defined staircase is observed. At the eddy flanks, however, the geostrophic shear is high and a double-diffusive step structure is not observed, even though the vertical density ratio (and \overline{Tu}) are in the appropriate ranges for DC instability. Below $\overline{Ri}_g \sim 100$, the step structure is not observed. For the SF regime at the bottom of the eddy, an SF staircase is observed in regions where shear is weakest, while at the same time, the density ratio and \overline{Tu} are in a range amenable to the SF instability. In high shear zones, where \overline{Tu} is in the SF-susceptible range, a robust staircase is not observed (where $\overline{Ri}_g < O(100)$), similar to the DC case.

Estimates of \overline{Ri}_g at the flanks are 2 orders of magnitude above the putative criterion of $Ri < 1/4$ for shear-driven mixing. Of course, ageostrophic velocities that are not reflected in a geostrophic Richardson number are likely to contribute to shear. Future analyses of velocity measurements (instead of needing to rely on geostrophic shear calculations from the density field) are required. Velocity measurements are needed to understand the mechanism of staircase destruction with a possible scenario being that the background shear (i.e., the geostrophic shear due to the eddy) can be amplified at double-diffusive interfaces (as described by *Padman* [1994]). Further, mesoscale eddies can be regions of internal wave critical layer absorption in which momentum is transferred to the mean flow (i.e., eddy rotation speeds and associated shear increase). This can lead to higher-velocity shear associated with the presence of the eddy than is reflected in the density structure, and associated instability and mixing [*Padman et al.*, 1990]. In this case, bulk Richardson numbers would be much lower than the geostrophic Richardson numbers computed here.

Assuming purely double-diffusive mixing in the vicinity of the eddy core and purely turbulent mixing in the high shear zones (at the flanks), we estimated the distribution of heat and salt fluxes across the eddy and placed an upper bound on the eddy lifetime of around 4–9 years. Different double-diffusive flux parameterizations may yield flux estimates that differ by about a factor of 2 [see e.g., *Robertson et al.*, 1995; *Kelley et al.*, 2003; *Timmermans et al.*, 2008a]. Taking into account a factor of 2 uncertainty in double-diffusive

fluxes from the core, where fluxes are over about 1/4 of the eddy area, introduces an uncertainty in the time for dissipation of the heat and salt anomaly of about 20%. Another source of error in the double-diffusive flux parameterization is the influence of the Earth's rotation, which can lead to reduced heat fluxes; however, staircase interfaces are sufficiently thin in this region that this should not be a factor [Carpenter and Timmermans, 2014]. Note also that considering typical interface thicknesses of about 10 cm in the region [Padman and Dillon, 1987; Timmermans et al., 2008a], it is possible that a single "interface" sampled by the ITP (25 cm vertical resolution) may in fact contain multiple unresolved layers. In this case, the heat flux estimated from the double-diffusive 4/3-flux parameterization is an upper bound, with the actual flux being smaller by a factor $\sim(1/(n+1))^{4/3}$, where n is the number of unresolved layers within an interface. Given the vertical resolution of the ITP measurements, we expect no more than about one unresolved layer within an "interface." This amounts to a heat flux that is smaller than our estimated value by a factor of about 0.4, equating to an uncertainty in eddy lifetime of about 20%.

Our estimated eddy decay time scale is comparable to the decay time of halocline eddies in the Canada Basin (e.g., of order a few years to 10 years [Padman et al., 1990; Timmermans et al., 2008b; Zhao et al., 2014]). Note that Padman et al. [1990] infer 10 years for an upper-halocline cyclone based on the total energy and measured dissipation rates. However, lateral fluxes due to the divergence of vertical heat and salt fluxes across the eddy, and lateral intrusive exchange likely drives an even faster decay ranging from months to a few years (depending on lateral diffusivity values). Turbulence reduces the vertical temperature, salinity, and density gradients, while double diffusion reduces the vertical temperature and salinity gradients, and increases the vertical density gradient. Thus, as the core of the eddy becomes lighter (considering that SF fluxes at its base dominate over DC fluxes at its top), this competes with turbulent mixing at the flank regions. These differing mixing processes enhance lateral density gradients, and likely drive enhanced lateral diffusivities that would further shorten the eddy lifetime.

This study has demonstrated the significant role of double-diffusive processes in speeding up the decay of an AW eddy. We suggest that the shortened eddy lifetimes may be one reason why AW eddies are not observed as frequently as halocline eddies [e.g., Zhao et al., 2014] that are not subject to double-diffusive mixing. If so, this has important implications to the distribution of AW heat in the Arctic Ocean, suggesting a mechanism for efficient mixing after transfer from the baroclinically unstable AW boundary current. The changing impacts of the competing mixing processes as the eddy evolves (e.g., with reduced shear at the flanks as the eddy spins down) require further investigation, which will be greatly aided by direct velocity measurements in the vicinity of an AW eddy.

Acknowledgments

The Ice-Tethered Profiler data were collected and made available by the Ice-Tethered Profiler Program based at the Woods Hole Oceanographic Institution [Krishfield et al., 2008; Toole et al., 2011]; data are available at <http://www.whoi.edu/itp/data>. Partial support was provided by the National Science Foundation Division of Polar Programs under award 1350046. We thank Laurie Padman and Barry Ruddick for their constructive and thoughtful reviews. We acknowledge support and valuable discussions during the Forum for Arctic Modeling and Observational Synthesis (FAMOS) and the FAMOS School for Young Arctic Scientists.

References

- Carmack, E. C., K. Aagaard, J. H. Swift, R. G. Perkin, F. A. McLaughlin, R. W. Macdonald, and E. P. Jones (1998), Thermohaline transitions, in *Physical Processes in Lakes and Oceans*, pp. 179–186, AGU, Washington, D. C.
- Carpenter, J., and M.-L. Timmermans (2012), Deep mesoscale eddies in the Canada Basin, Arctic Ocean, *Geophys. Res. Lett.*, *39*, L20602, doi:10.1029/2012GL053025.
- Carpenter, J., and M.-L. Timmermans (2014), Does rotation influence double-diffusive fluxes in polar oceans?, *J. Phys. Oceanogr.*, *44*(1), 289–296.
- Dillon, T. M. (1982), Vertical overturns: A comparison of Thorpe and Ozmidov length scales, *J. Geophys. Res.*, *87*(C12), 9601–9613.
- Dmitrenko, I. A., S. A. Kirillov, V. Ivanov, and R. Woodgate (2008), Mesoscale Atlantic water eddy off the Laptev Sea continental slope carries the signature of upstream interaction, *J. Geophys. Res.*, *113*, C07005, doi:10.1029/2007JC004491.
- Flór, J.-B. (2010), *Fronts, Waves and Vortices in Geophysical Flows*, vol. 805, 192 pp., Springer-Verlag, Berlin Heidelberg.
- Galbraith, P. S., and D. E. Kelley (1996), Identifying overturns in ctd profiles, *J. Atmos. Oceanic Technol.*, *13*(3), 688–702.
- Gregg, M. C., and T. B. Sanford (1987), Shear and turbulence in thermohaline staircases, *Deep Sea Res., Part A*, *34*(10), 1689–1696.
- Guthrie, J. D., J. H. Morison, and I. Fer (2013), Revisiting internal waves and mixing in the Arctic Ocean, *J. Geophys. Res. Oceans*, *118*, 3966–3977, doi:10.1002/jgrc.20294.
- Halle, C., and R. Pinkel (2003), Internal wave variability in the Beaufort Sea during the winter of 1993/1994, *J. Geophys. Res.*, *108*(C7), 3210, doi:10.1029/2000JC000703.
- Hebert, D. (1988), Estimates of salt-finger fluxes, *Deep Sea Res., Part A*, *35*(12), 1887–1901.
- Hebert, D., N. Oakey, and B. Ruddick (1990), Evolution of a Mediterranean salt lens: Scalar properties, *J. Phys. Oceanogr.*, *20*(9), 1468–1483.
- Inoue, R., H. Yamazaki, F. Wolk, T. Kono, and J. Yoshida (2007), An estimation of buoyancy flux for a mixture of turbulence and double diffusion, *J. Phys. Oceanogr.*, *37*(3), 611–624.
- Ivey, G., K. Winters, and J. Koseff (2008), Density stratification, turbulence, but how much mixing?, *Annu. Rev. Fluid Mech.*, *40*(1), 169–184.
- Jackson, J. M., S. E. Allen, F. McLaughlin, R. Woodgate, and E. Carmack (2011), Changes to the near-surface waters in the Canada Basin, Arctic Ocean from 1993–2009: A basin in transition, *J. Geophys. Res.*, *116*, C10008, doi:10.1029/2011JC007069.
- Johnson, H. L., and C. Garrett (2004), Effects of noise on Thorpe scales and run lengths, *J. Phys. Oceanogr.*, *34*(11), 2359–2372.
- Jones, E., B. Rudels, and L. Anderson (1995), Deep waters of the Arctic Ocean: Origins and circulation, *Deep Sea Res., Part I*, *42*(5), 737–760.
- Kelley, D., H. Fernando, A. Gargett, J. Tanny, and E. Özsoy (2003), The diffusive regime of double-diffusive convection, *Prog. Oceanogr.*, *56*(3), 461–481.

- Kelley, D. E. (1990), Fluxes through diffusive staircases: A new formulation, *J. Geophys. Res.*, *95*(C3), 3365–3371.
- Krishfield, R., J. Toole, A. Proshutinsky, and M.-L. Timmermans (2008), Automated Ice-Tethered Profilers for seawater observations under pack ice in all seasons, *J. Atmos. Oceanic Technol.*, *25*(11), 2091–2105.
- Manley, T., and K. Hunkins (1985), Mesoscale eddies of the Arctic Ocean, *J. Geophys. Res.*, *90*(C3), 4911–4930.
- McLaughlin, F. A., E. C. Carmack, W. J. Williams, S. Zimmermann, K. Shimada, and M. Itoh (2009), Joint effects of boundary currents and thermohaline intrusions on the warming of Atlantic water in the Canada Basin, 1993–2007, *J. Geophys. Res.*, *114*, C00A12, doi:10.1029/2008JC005001.
- Melling, H., R. Lake, D. Topham, and D. Fissel (1984), Oceanic thermal structure in the western Canadian arctic, *Cont. Shelf Res.*, *3*(3), 233–258.
- Merryfield, W. J. (2000), Origin of thermohaline staircases, *J. Phys. Oceanogr.*, *30*(5), 1046–1068.
- Merryfield, W. J. (2002), Intrusions in double-diffusively stable Arctic waters: Evidence for differential mixing?, *J. Phys. Oceanogr.*, *32*(5), 1452–1459.
- Morell, J. M., J. E. Corredor, and W. J. Merryfield (2006), Thermohaline staircases in a Caribbean eddy and mechanisms for staircase formation, *Deep Sea Res., Part II*, *53*(1), 128–139.
- Moum, J. (1996), Efficiency of mixing in the main thermocline, *J. Geophys. Res.*, *101*(5), 12,057–12,069.
- Neal, V. T., and S. Neshyba (1973), Microstructure anomalies in the Arctic Ocean, *J. Geophys. Res.*, *78*(15), 2695–2701.
- Osborn, T. (1980), Estimates of the local rate of vertical diffusion from dissipation measurements, *J. Phys. Oceanogr.*, *10*(1), 83–89.
- Padman, L. (1994), Momentum fluxes through sheared oceanic thermohaline steps, *J. Geophys. Res.*, *99*(C11), 22,491–22,499.
- Padman, L., and T. M. Dillon (1987), Vertical heat fluxes through the Beaufort Sea thermohaline staircase, *J. Geophys. Res.*, *92*(C10), 10,799–10,806.
- Padman, L., and T. M. Dillon (1988), On the horizontal extent of the Canada Basin thermohaline steps, *J. Phys. Oceanogr.*, *18*(10), 1458–1462.
- Padman, L., and T. M. Dillon (1989), Thermal microstructure and internal waves in the Canada Basin diffusive staircase, *Deep Sea Res., Part A*, *36*(4), 531–542.
- Padman, L., M. Levine, T. Dillon, J. Morison, and R. Pinkel (1990), Hydrography and microstructure of an Arctic cyclonic eddy, *J. Geophys. Res.*, *95*(C6), 9411–9420.
- Peltier, W., and C. Caulfield (2003), Mixing efficiency in stratified shear flows, *Annu. Rev. Fluid Mech.*, *35*(1), 135–167.
- Perkin, R., and E. Lewis (1984), Mixing in the West Spitsbergen current, *J. Phys. Oceanogr.*, *14*(8), 1315–1325.
- Pickart, R. S., T. J. Weingartner, L. J. Pratt, S. Zimmermann, and D. J. Torres (2005), Flow of winter-transformed Pacific water into the Western Arctic, *Deep Sea Res., Part II*, *52*(24), 3175–3198.
- Polyakov, I. V., et al. (2011), Fate of early 2000s Arctic warm water pulse, *Bull. Am. Meteorol. Soc.*, *92*(5), 561–566.
- Proshutinsky, A., R. Krishfield, M.-L. Timmermans, J. Toole, E. Carmack, F. McLaughlin, W. J. Williams, S. Zimmermann, M. Itoh, and K. Shimada (2009), Beaufort Gyre freshwater reservoir: State and variability from observations, *J. Geophys. Res.*, *114*, C00A10, doi:10.1029/2008JC005104.
- Radko, T. (2003), A mechanism for layer formation in a double-diffusive fluid, *J. Fluid Mech.*, *497*, 365–380.
- Radko, T. (2013), *Double-Diffusive Convection*, 344 pp., Cambridge University Press, N. Y.
- Rainville, L., and P. Winsor (2008), Mixing across the Arctic ocean: Microstructure observations during the Beringia 2005 expedition, *Geophys. Res. Lett.*, *35*, L08606, doi:10.1029/2008GL033532.
- Rippeth, T. P., B. J. Lincoln, Y.-D. Lenn, J. M. Green, A. Sundfjord, and S. Bacon (2015), Tide-mediated warming of Arctic halocline by Atlantic heat fluxes over rough topography, *Nat. Geosci.*, *8*(3), 191–194.
- Robertson, R., L. Padman, and M. D. Levine (1995), Fine structure, microstructure, and vertical mixing processes in the upper ocean in the western Weddell Sea, *100*(C9), 18,517–18,535.
- Ruddick, B. (1983), A practical indicator of the stability of the water column to double-diffusive activity, *Deep Sea Res., Part A*, *30*(10), 1105–1107.
- Schmitt, R. W. (1979), Flux measurements on salt fingers at an interface, *J. Mar. Res.*, *37*(3), 419–436.
- Schmitt, R. W. (1981), Form of the temperature-salinity relationship in the Central Water: Evidence for double-diffusive mixing, *J. Phys. Oceanogr.*, *11*(7), 1015–1026.
- Smyth, W., J. Moum, and D. Caldwell (2001), The efficiency of mixing in turbulent patches: Inferences from direct simulations and microstructure observations, *J. Phys. Oceanogr.*, *31*(8), 1969–1992.
- Stern, M. E. (1960), The Salt-Fountain and thermohaline convection, *Tellus*, *12*(2), 172–175.
- St. Laurent, L., and R. W. Schmitt (1999), The contribution of salt fingers to vertical mixing in the North Atlantic Tracer Release Experiment, *J. Phys. Oceanogr.*, *29*(7), 1404–1424.
- Thorpe, S. A. (2005), *The Turbulent Ocean*, 439 pp., Cambridge University Press, N. Y.
- Timmermans, M.-L., C. Garrett, and E. Carmack (2003), The thermohaline structure and evolution of the deep waters in the Canada Basin, Arctic Ocean, *Deep Sea Res., Part I*, *50*(10), 1305–1321.
- Timmermans, M.-L., J. Toole, R. Krishfield, and P. Winsor (2008a), Ice-Tethered Profiler observations of the double-diffusive staircase in the Canada Basin thermocline, *J. Geophys. Res.*, *113*, C00A02, doi:10.1029/2008JC004829.
- Timmermans, M.-L., J. Toole, A. Proshutinsky, R. Krishfield, and A. Plueddemann (2008b), Eddies in the Canada Basin, Arctic Ocean, observed from Ice-Tethered Profilers, *J. Phys. Oceanogr.*, *38*(1), 133–145.
- Timmermans, M.-L., et al. (2014), Mechanisms of Pacific Summer Water variability in the Arctic's Central Canada Basin, *J. Geophys. Res. Oceans*, *119*, 7523–7548, doi:10.1002/2014JC010273.
- Toole, J., R. Krishfield, M.-L. Timmermans, and A. Proshutinsky (2011), The Ice-Tethered Profiler: Argo of the Arctic, *Oceanography*, *24*(3), 126–135.
- Turner, J. (1965), The coupled turbulent transports of salt and heat across a sharp density interface, *Int. J. Heat Mass Transfer*, *8*(5), 759–767.
- van Gastel, P., and J. L. Pelegrí (2004), Estimates of gradient Richardson numbers from vertically smoothed data in the Gulf Stream region, *Sci. Mar.*, *68*(4), 459–482.
- von Appen, W.-J., R. S. Pickart, K. H. Brink, and T. W. Haine (2014), Water column structure and statistics of Denmark Strait Overflow Water cyclones, *Deep Sea Res., Part I*, *84*, 110–126.
- Walsh, D., and E. Carmack (2003), The nested structure of Arctic thermohaline intrusions, *Ocean Modell.*, *5*(3), 267–289.
- Watanabe, E., et al. (2014), Enhanced role of eddies in the Arctic marine biological pump, *Nat. Commun.*, *5*, 3950.

- Woodgate, R. A., K. Aagaard, R. D. Muench, J. Gunn, G. Björk, B. Rudels, A. Roach, and U. Schauer (2001), The Arctic Ocean boundary current along the Eurasian slope and the adjacent Lomonosov Ridge: Water mass properties, transports and transformations from moored instruments, *Deep Sea Res., Part I*, 48(8), 1757–1792.
- Woodgate, R. A., K. Aagaard, J. H. Swift, W. M. Smethie, and K. K. Falkner (2007), Atlantic water circulation over the Mendeleev Ridge and Chukchi Borderland from thermohaline intrusions and water mass properties, *J. Geophys. Res.*, 112, C02005, doi:10.1029/2005JC003416.
- Zhao, M., M.-L. Timmermans, S. Cole, R. Krishfield, A. Proshutinsky, and J. Toole (2014), Characterizing the eddy field in the Arctic Ocean halocline, *J. Geophys. Res.*, 119, 8800–8817, doi:10.1002/2014JC010488.